Application of Theory to Simulations of Observed Cases of Orographically Forced Convective Rainfall

MARIO MARCELLO MIGLIETTA

ISAC-CNR, Lecce, and ISE-CNR, Verbania Pallanza, Italy

RICHARD ROTUNNO

National Center for Atmospheric Research, Boulder, Colorado*

(Manuscript received 28 September 2011, in final form 3 January 2012)

ABSTRACT

In two recent papers, the authors reported on numerical simulations of conditionally unstable flows past an idealized mesoscale mountain ridge. These idealized simulations, which were performed with a three-dimensional, explicitly cloud-resolving model, allowed the investigation of simulated precipitation characteristics as a function of the prescribed environment. The numerical solutions were carried out for a uniform wind flowing past a bell-shaped ridge and using an idealized unstable sounding with prescribed values of the relevant parameters.

In the present work the application of these theoretical results to observed cases of orographically forced convective rainfall including the Big Thompson flood (1976, Colorado), the Oahu flood (1974, Hawaii), and the Gard flood (2002, France) is reported. Specifically, numerical simulations have been carried out using observed and idealized soundings relevant to these cases but with idealized topography. It is found that using the observed soundings, but with idealized constant-wind profiles, the simulated rain rates fit reasonably well within the previous theoretically derived parameter space for intense orographic convective rainfall. However, in order to reproduce larger rainfall rates, in closer agreement with observations, in the first two cases it was necessary to initialize the sounding with a wind profile characterized by low-level flow toward the mountain with weak flow aloft (as observed for the across-mountain wind component). For the Gard case, the situation was more complex and it is found unlikely that the situation can be reduced to a simple two-dimensional problem.

1. Introduction

Orographic precipitation results from a complex combination of different scales of motion: moist, large-scale flow; mesoscale orographically induced lifting; and small-scale processes such as convection, turbulence, and microphysics (Rotunno and Houze 2007). While the orographic precipitation problem in stable and neutral atmospheric conditions is fairly well understood, the problem in the unstable case is still far from being solved and presents significant challenges to the successful numerical prediction of this kind of event.

The occurrence of heavy-rain convective events over complex orography is well documented in different parts of the world (see Richard et al. 2007 for a review). However, the timing, evolution, and location of these events can differ greatly from case to case; for example, the heaviest concentration of rainfall may affect the foothills (Caracena et al. 1979), the region just upwind (Delrieu et al. 2005), or even the downwind side (Schroeder 1977) of a mountain ridge; in addition, the flow can be deflected by mountain chains or channeled by gaps (Buzzi and Foschini 2000).

Large rainfall amounts are generally associated with the persistence of convective systems in a limited region for several hours. In such systems, convective cells often have trajectories that carry them over the same location many times (Chappell 1986, p. 289). For this to occur,

* The National Center for Atmospheric Research is sponsored by the National Science Foundation.

Corresponding author address: Mario Marcello Miglietta, CNR-ISAC, Strada Provinciale Lecce-Monteroni, 73100 Lecce, Italy.
E-mail: m.miglietta@isac.cnr.it

DOI: 10.1175/MWR-D-11-00253.1

outflows from downdrafts either do not move away from the heavy rain, or are not present with the depth nor density difference to initiate cells in locations away from the affected region (Davis 2001).

Orographic convective triggering and maintenance of such systems has been proposed to occur through different mechanisms—for example, orographic uplift (Yu et al. 2007), uplift over orographically blocked flow (Neiman et al. 2002; Yu and Hsieh 2009), formation of areas of convergence (Rotunno and Ferretti 2001), local convergence at low-level-flow separation lines (Wang et al. 2000), thermal forcing (Romero et al. 2000), and/or the remote effects of mountain waves (Grossman and Durran 1984). In some cases, the orography serves as a fixed lifting mechanism to force moist flow to its lifting condensation level and ''anchors'' the system. In addition, the complex nature of the terrain may result in localized areas of persistent convergence that repeatedly triggers convection over the same locations (Kodama and Barnes 1997).

On the one hand, similarities have been detected in the synoptic environments conducive to some disruptive upslope convective events, such as a short wave aloft combined with a postfrontal band of conditionally unstable air, and weak middle- and upper-tropospheric currents (Pontrelli et al. 1999, their Fig. 25). On the other hand, the importance of specifically mesoscale ingredients, such as the moist and conditionally unstable low-level jets, has been examined in particular cases of complex terrain to assess their ability to focus deep convection over the same area for several hours (e.g., the Gard flood over southern France; see Ducrocq et al. 2008).

Identifying the conditions favorable for a statistically stationary convective system over orography can be particularly difficult, as one can envision scenarios in which deep convective cells do not concentrate their precipitation in the same location. After their formation, cells may move according to the wind aloft and thus produce rain in another location, or, rather, a density current may develop and trigger cells far from the mountain. In such cases, convectively induced cold pools and outflows can be very important for the propagation of convective systems and/or to focus, together with the orography, convective-cell development in a confined area (Senesi et al. 1996; Romero et al. 2000). A better understanding of the problem first requires the identification of the most important environmental variables. In an attempt to find those parameters in a simplified theoretical context, the authors (Miglietta and Rotunno 2009, hereafter MR09, and Miglietta and Rotunno 2010, hereafter MR10) have recently reported on a series of idealized three-dimensional explicitly cloud-resolving simulations of conditionally unstable flow past a two-dimensional ridge. The present study represents our attempt to apply those results to observed cases of intense convective orographic rainfall.

As the analyzed events are generally very complex, because of the three dimensionality of the flow and of the topography, the time evolution of the synoptic situation, etc., we cannot expect to represent the observed rainfall with the extremely simplified setup we used. Rather, we have tried to apply the results of our previous studies to three soundings—representative of the upstream conditions that occurred in heavy-rain events—that are somewhat different from the Weisman and Klemp (1982) profiles used in those papers in order to see to what extent these cases are consistent with our theory. We have also explored the sensitivity of the peak rainfall to some of the nondimensional parameters considered in our theory and the importance of an additional parameter, the wind shear, which has not been considered up to now.

In section 2 we review the theoretical background for the current study. Section 3 recounts our attempts to simulate several well-documented cases within the present idealized context. Section 4 summarizes the conclusions and outlines our view of the next steps to be taken.

2. Theoretical background

As noted above, MR09 and MR10 have recently reported on a series of three-dimensional numerical simulations of conditionally unstable flows impinging on a two-dimensional mesoscale mountain ridge. The simulations were performed with a three-dimensional explicitly cloud-resolving model [Cloud Model 1 (CM1), release 8; Bryan and Fritsch 2002] in order to investigate the statistically stationary (along-ridge averaged) features of the solution precipitation characteristics. CM1 was selected because it conserves mass and energy better than other modern cloud models. Also, CM1 was designed specifically to do very large domain simulations using high resolution and therefore has comparatively little memory overhead.

MR09 considered an archetypal sounding for convective instability—the Weisman and Klemp (1982; WK) sounding, with a uniform wind U flowing past a bell-shaped ridge of height h_m and half-width a—and specified the convective available potential energy (CAPE), downdraft CAPE (DCAPE),[1] level of free convection (LFC), tropopause height h_t, and static stability N^2. MR09 carried out these numerical simulations by varying the

[1] DCAPE is a measure of the cold-pool buoyancy produced by rainy downdrafts (see Gilmore and Wicker 1998).

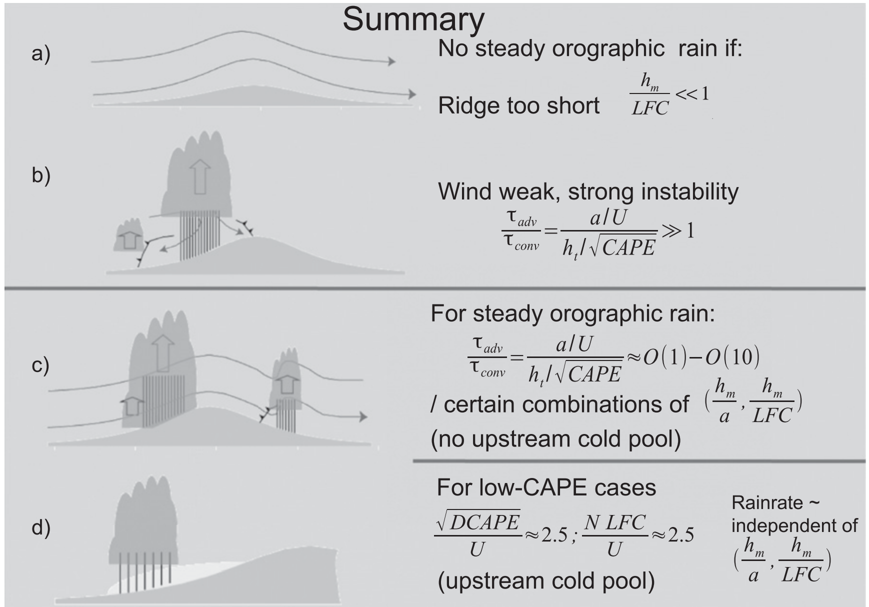

FIG. 1. Summary of the solutions obtained in MR09 and MR10.

different parameters associated with the sounding and with the orography and then measured the convective response in terms of along-ridge averaged rainfall location and intensity.

Dimensional analysis of the results revealed that the maximum nondimensional rainfall rate $R_m/\rho_{vs}U$ (Rotunno and Ferretti 2001; Miglietta and Rotunno 2006), where ρ_{vs} is the saturation vapor density at the ground, mainly depends on three nondimensional numbers. One is the ratio of mountain height to the level of free convection h_m/LFC, the second is the slope parameter h_m/a, and the third is the ratio of an advective time scale $\tau_a = a/U$ to a convective time scale $\tau_c = h_t/(\text{CAPE})^{1/2}$ (the time that convective elements take to grow and produce rain at the ground).

With the benefit of tens of simulations, MR09 developed the following conceptual model for large convective orographic rainfall: 1) h_m/LFC should be greater than a threshold value (in order to trigger convection); 2) τ_a/τ_c should not be too large (~1–10) (in order to generate a cold pool that will not propagate far away upwind of the ridge); and 3) for given τ_a/τ_c and h_m/LFC larger than or approximately equal to 0.3, there is an optimal range of h_m/a (MR09, their Fig. 15; MR10, their Figs. 2 and 3). A summary of the solution features obtained in MR09 and MR10 is shown in Fig. 1.

Subsequently, the work was extended (MR10) to take into account further parameter variations that were not considered in MR09. Specifically, MR10 extended the MR09 analysis to cover larger regions of the thermodynamic parameter space, in particular covering a wider range of values of CAPE. MR10 found the precipitation produced in low-CAPE, moderate-wind experiments does not fit the functional dependence for rain rate amount and location proposed in MR09; further analysis suggested that two additional nondimensional parameters—$\text{DCAPE}^{1/2}/U$ (which represents a measure of the propagation of the downdraft-produced cold pool with respect to environmental-flow advection) and NLFC/U (which estimates the deceleration of the environmental wind induced by the cold pool)—should be taken into account.

To test the applicability of the above-described work, we have performed a series of three-dimensional high-resolution numerical simulations relevant to observed cases of flooding-rain events using the same simplified context as in our previous studies. The numerical setup is the same as MR09 and MR10, so we will refer to those papers for further details and limit our description here to the essential information. The domain is 320 km long and 20 km wide with a horizontal grid spacing of 250 m; the vertical extent of the domain is 20 km, with 59 levels having a vertical grid spacing varying from 250 m close to the ground to 500 m in the upper levels. The setup has been chosen to carry out computations at reasonable cost, without significant sacrifice of physical realism: for example, the 20-km domain width was determined by carrying out solutions for a smaller domain width and then increasing it until no substantial changes were observed in the solutions. The orography is prescribed by a bell-shaped mountain, with small-amplitude irregularities added in order to break the y symmetry of the initial condition and obtain a fully three-dimensional solution. The random irregularities of the topography may affect single-cell generation, but not the statistically stationary fields, which are obtained after averaging in the y direction and over a time window of 5 h (such a period is long enough compared to the lifetime of the individual cells). Thus, in this context, the effect of the individual irregularities can be considered irrelevant. The observed soundings, after some smoothing and simplifications as discussed in section 3, are used to initialize CM1. Thus we will compare the simulations of these observed cases of orographically forced convective rainfall with the theory developed in MR09 and MR10.

Finally, as low-level flow toward the orography with weak winds aloft is often present in cases of orographically forced heavy convective rain, we will also perform additional experiments including such 2D wind profiles and consider its effect on the simulated precipitation features. However, for these latter experiments we have not yet developed a theoretical background, since in MR09 and MR10 we had so many parameters to consider that we postponed the analysis of the effect of variable wind $U(z)$ to a future study. Thus, orographic-flow experiments with the prototypal Weisman–Klemp sounding, but with typical wind profiles $U = U(z)$, will be discussed in a following article.

3. Case studies

In the present section, different case studies with strong orographic convection are analyzed and discussed in the framework of the theory developed in MR09 and MR10. These events, which occurred in different parts of the world, show different characteristics and have been thoroughly documented because of their impact. Here, we try to see how far we can go toward simulating them within the present simplified context.

The present endeavor presented several challenges. Generally, the meteorological situation is nonstationary and spatially varying and the topography is three dimensional; thus, the idealization of using a single sounding upstream of a two-dimensional mountain can be an oversimplification of the problem. However, even if one stipulates the applicability of a single sounding, the results can still be quite sensitive to what may appear to be minor variations in the sounding. Herein we present an account of our attempts to use real soundings with simplified orography to see if one can describe at least the gross features of observed orographic convective heavy-rain events.

In the observed cases only the maximum instantaneous rain rate of a cell with limited duration is reported. In the simulations, a statistically steady state can be established that, by definition, is of infinite duration. Thus it is not possible to establish a one-to-one correspondence between observed and simulated rainfall peak R_m. However, we can compare different simulations to each other and ask which produces the largest R_m for sounding variations within the observed range of variability and thus assess what conditions might have led to the largest rain rates and presumably intense rainfall in the observed cases. Flooding, however, is a result of repeating rain cells over a specific location; in the case of orographic precipitation, the distance from the mountain summit of the maximum statistically steady rain rate, X_m, is the appropriate datum for comparison with the observed region of flooding rains.

a. Big Thompson

First we consider the Big Thompson Canyon (BIGT) flood, which involved orographically forced convection over the Rocky Mountains as discussed in Caracena et al. (1979). The BIGT case was characterized by a strong low-level easterly flow, oriented nearly normal to the orography, that advected a very moist, conditionally unstable air mass toward the eastern side of Front Range of the Rocky Mountains, about 40 km north of Boulder, Colorado, on 31 July–1 August 1976 (Fig. 2). According to Caracena et al. (1979), orographic uplift provided the necessary destabilization to trigger convection, and a very light upper-level southerly wind allowed the storm complex to remain nearly stationary (Fig. 3). Heavy precipitation focused on a narrow corridor in the foothills, producing devastating flash floods, while no intense precipitation occurred at higher elevations. At least 139 people were killed and property damage of about \$35.5 million (U.S. dollars) occurred. A detailed analysis of the synoptic conditions of the prestorm stage can be found in Maddox et al. (1978).

1) Experiments with U = const

In our preliminary attempts using the smoothed profile reported in Yoshizaki and Ogura (1988), their Fig. 2a, and the constant-wind $U = 13$ m s^{-1}, we found that the rainfall rate (experiment BIGT1 in Table 1) was much smaller than that indicated by the observations (Caracena et al. 1979 calculated adjusted rainfall rates ~150 mm h^{-1} in the flooding area during the most intense part of the storm). In a further attempt, we initialized the model with the interpolated sounding (representative of upstream conditions), shown in Caracena et al. (1979), their Fig. 5b, and the constant-wind $U = 10$ m s^{-1} (experiment BIGT2 in Table 1). Also in this case the rainfall rate was very small.

However, that sounding contains several thermal inversions, which could prevent the triggering of convection, and very dry midlevels, which would produce overly

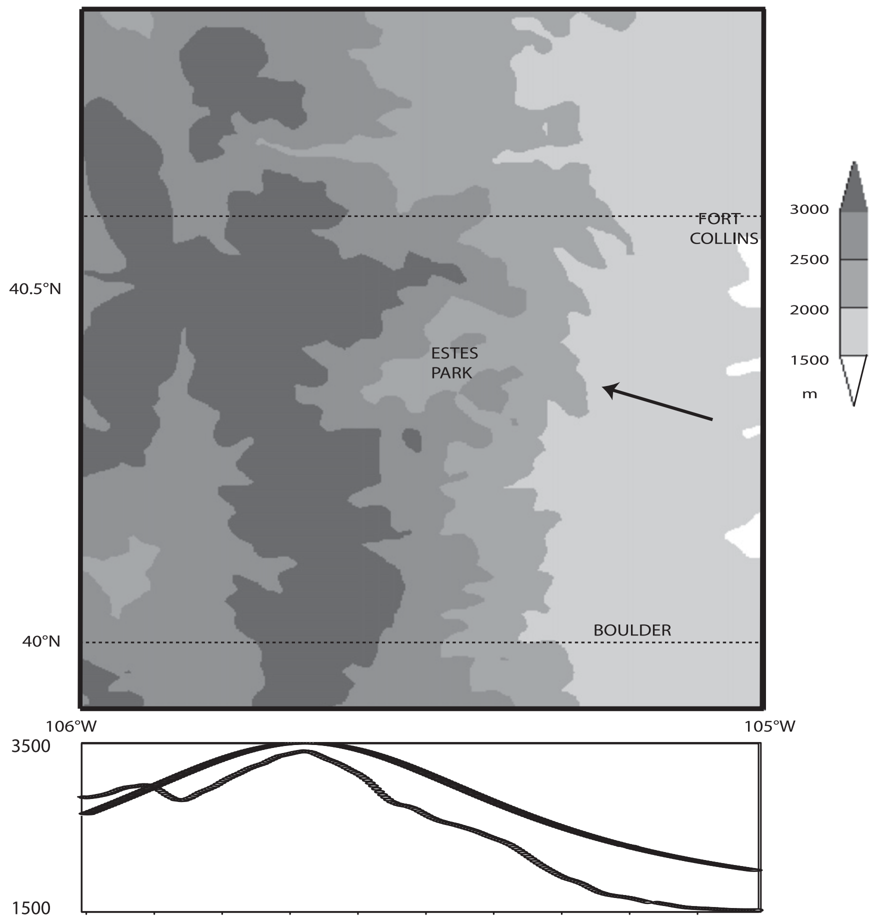

FIG. 2. (top) Topography of the region affected by the Big Thompson flash flood. Terrain contours (m MSL) are shaded. The arrow represents the low-level-flow direction. (bottom) The average mountain profile in the area of maximum rainfall, between 40° and 40.6°N and from 106° to 105°W (indicated with the dotted box in the top), is shown for sake of comparison with the idealized profile.

strong cold pools; thus, we decided to initialize the model with our own smoothed profiles shown in Fig. 3. After such simplifications, an idealized, smooth sounding, generated from the real profile, is used to test the theory. We used $U = 10\ \mathrm{m\ s^{-1}}$, the average wind speed throughout the vertical column, and a bell-shaped mountain with $h_m = 1800$ m and $a = 30$ km (experiment BIGT3 in Table 1). We also tested slight increases in the humidity content between 800 and 700 hPa (experiment BIGT4 in Table 1 and dashed lines in Fig. 3) or a different mountain shape [the same upstream width but with a downstream width twice as large (experiment BIGT5) and thus closer to the real mountain shape], but in all cases the peak rainfall (approximately $10\ \mathrm{mm\ h^{-1}}$) was much smaller than observed.

Based on the findings in MR09 and MR10, we looked for slight variations in the parameters U, h_m, and a (but still reasonably close to those of the BIGT case) that would produce stronger precipitation. As shown in Table 1, the two simulations BIGT6 ($U = 10\ \mathrm{m\ s^{-1}}$) and BIGT7 ($U = 7\ \mathrm{m\ s^{-1}}$) belong to a region of large h_m/a and h_m/LFC for small/intermediate τ_a/τ_c (cf. MR10, their Fig. 3). With respect to experiment BIGT3, these two experiments had slightly increased rainfall, because of the presence of deeper convective cells, and the peak is shifted downstream. In particular, in experiment BIGT7, a smaller wind speed produced a larger nondimensional rainfall, although the changes in absolute precipitation were relatively minor.

To evaluate how much the choice of the value of the constant wind affected the rainfall rate, we performed three additional experiments with exactly the same setup but with the different wind speeds $U = 5\ \mathrm{m\ s^{-1}}$, $10\ \mathrm{m\ s^{-1}}$, and $17\ \mathrm{m\ s^{-1}}$ (experiments BIGT9, BIGT10, and BIGT11). In experiment BIGT9, a cold pool propagated far upstream and no stationary rainfall was simulated above the mountain. Both of the other two cases show results similar to the previous experiments with uniform wind profiles;

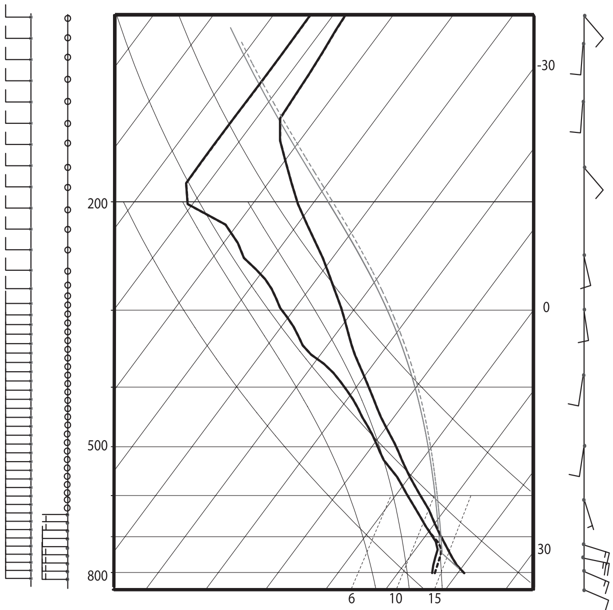

FIG. 3. The idealized profiles of temperature and dewpoint used in our experiments BIGT3 and BIGT5–7 (solid, thick black lines) and BIGT4 and BIGT8–12 (dashed, where not coincident with the solid line, thick black lines). The bold (respectively, solid and dashed) gray lines represent the pseudoadiabatic curves of a parcel lifted from the surface. The wind profiles used to initialize the atmosphere in the experiments BIGT10 and BIGT8 are shown on the left side together with the ''observed'' profile from Caracena et al. (1979), their Fig. 5b (on the right). A long wind barb stands for 10 m s^{-1} and a small one for 5 m s^{-1}.

Figs. 4a,b illustrate the solution for the case BIGT10. (The main difference between BIGT10 and BIGT11 is the distribution of the precipitation, which is shifted downstream in the latter case with stronger winds.)

2) EXPERIMENTS WITH $U = U(z)$

Considering that the observations show an intense low-level flow toward the mountains with weaker across-mountain flow aloft, we decided to introduce a similar wind profile in the initial condition. (Earth rotation is not included in the model; otherwise, a thermal wind balance should be prescribed in the approaching flow, resulting in considerable complications; e.g., Davolio et al. 2009.) Using the same thermodynamic sounding as in experiment BIGT10, we initialized the model with a wind profile having $U = 17$ m s^{-1} in the lowest four model levels (1500–2400 m) and $U = 0$ m s^{-1} above 4000 m (from level 11 above), with a linear interpolation defining $U(z)$ in between. The presence of the low-level flow dramatically increases the rainfall rate and the rainfall maximum is now located farther upstream (experiment BIGT8 in Table 1). Figures 4c,d show that this outcome is due to the presence of deep convective cells on the upstream side of the mountain, which are generated upstream as a consequence of lifting induced by a deep cold pool (the presence of a cold air pool caused by the evaporative cooling had been noted in the simulations in Yoshizaki and Ogura 1988). The presence of a low-level flow and calm aloft thus appear to be fundamental ingredients for the occurrence of larger rainfall rates in the simulations of this case (as concluded/hypothesized in observational studies).

The comparison of the constant-wind experiment BIGT10 with the low-level-flow-only experiment BIGT8 in Fig. 4 shows that the two solutions have a completely different behavior. In experiment BIGT10 (Fig. 4, top), the wind field indicates the presence of a mountain wave that warms the upper levels (by about 3 K, not shown)

TABLE 1. List of experiments relative to BIGT case. The simulations are identified with the name of the experiment; the values of U, h_m, a, CAPE, DCAPE, LFC, and N; the five nondimensional parameters identified in MR09 and MR10 [τ_a/τ_c, h_m/a, h_m/LFC, (DCAPE)$^{1/2}/U$, and NLFC/U]; and the values of the rainfall peak R_m and its location X_m are also shown together with the nondimensional parameters 10^2 $R_m/\rho_{vs}U$ and X_m/a.

Expt	U m s^{-1}	h_m m	a km	CAPE J kg^{-1}	DCAPE J kg^{-1}	LFC m	N s^{-1}	τ_a/τ_c	h_m/a	h_m/LFC	(DCAPE)$^{1/2}/U$	NLFC/U	R_m mm h^{-1}	X_m km	10^2 $R_m/\rho U$	X_m/a
BIGT1	13	1800	30	1550	920	1000	0.008	9.1	0.06	1.80	2.3	0.6	2	1	0.4	0.0
BIGT2	10	1800	30	2350	1020	2000	0.008	14.5	0.06	0.90	3.2	1.6	1	−8	0.2	−0.3
BIGT3	10	1800	30	2300	1013	1500	0.009	14.4	0.06	1.20	3.2	1.3	8	−6	1.8	−0.2
BIGT4	10	1800	30	2500	1017	1500	0.009	15.0	0.06	1.20	3.2	1.3	8	−6	1.8	−0.2
BIGT5	10	1800	30	2500	1017	1500	0.009	15.0	0.06	1.20	3.2	1.3	9	−13	2.1	−0.4
BIGT6	10	2000	13	2300	1013	1500	0.009	6.2	0.15	1.33	3.2	1.3	10	13	2.3	1.0
BIGT7	7	2000	13	2300	1013	1500	0.009	8.9	0.15	1.33	4.5	1.8	8	4	2.6	0.3
BIGT8		2000	30	2500	1017	1500	0.009		0.07	1.33			19	−19		−0.6
BIGT9	5	2000	30	2500	1017	1500	0.009	30.0	0.07	1.33	6.4	2.6	0		0.0	
BIGT10	10	2000	30	2500	1017	1500	0.009	15.0	0.07	1.33	3.2	1.3	8	−8	1.8	−0.3
BIGT11	17	2000	30	2500	1017	1500	0.009	8.8	0.07	1.33	1.9	0.8	11	10	1.5	0.3
BIGT12		2000	30	2500	1017	1500	0.009		0.07	1.33			0			

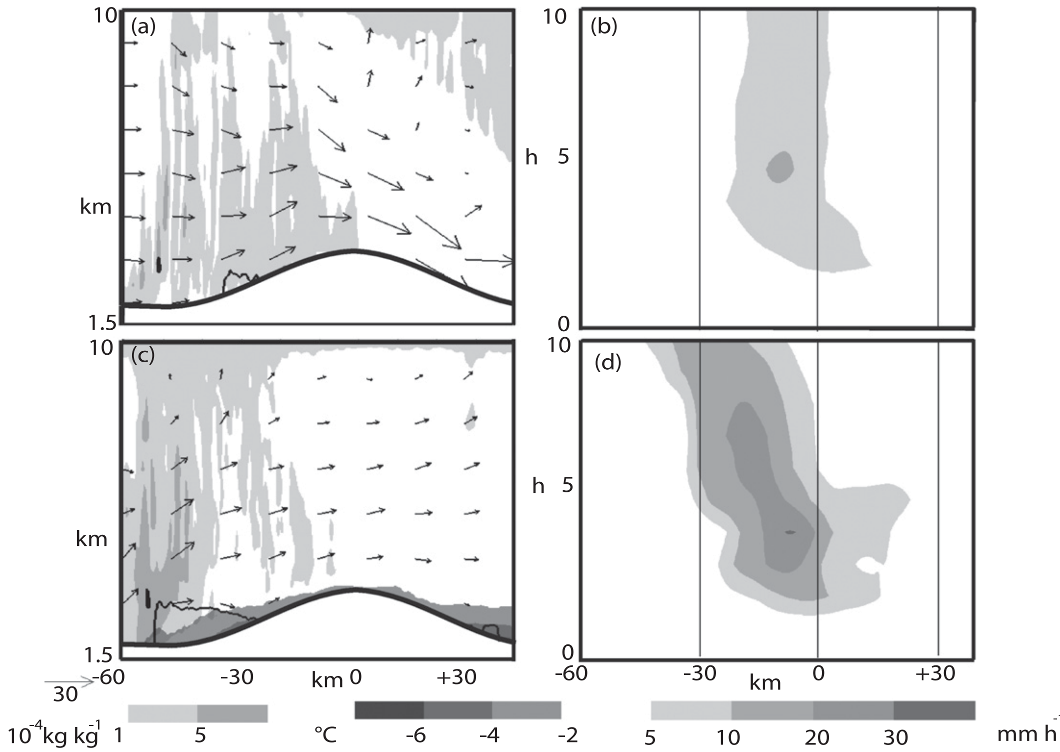

FIG. 4. (left) Vertical cross sections of the *y* average of potential temperature perturbation (dark shaded areas), cloud water plus ice content (light shaded areas), rainwater content (contour line for 0.2×10^{-3} kg kg^{-1}), and wind vectors (arrows) for experiments (a) BIGT10 and (c) BIGT8. The results are shown at the final integration time $t = 10$ h. (right) Hovmöller diagram of the *y* average of rain rate for experiments (b) BIGT10 and (d) BIGT8. The rain rate is calculated every 1 h from $t = 0$ to $t = 10$ h. The vertical lines represent the location of the ridge top and half width.

downstream and above the mountain, while experiment BIGT8 (Fig. 4, bottom) is characterized by a cold pool remaining on the mountain with no mountain wave or, at least, no strong descent in evidence. In the latter case, the uplift induced by the cold pool, together with the absence of upper-level advection, produces deep convective cells and shifts the rainfall peak farther upstream.

To test the sensitivity of the solution to the value of the low-level flow, experiment BIGT12 was done with the same numerical setup as in experiment BIGT8, but with $U = 10$ m s^{-1} instead of $U = 17$ m s^{-1} in the lower layer. In this case, a cold pool propagated upstream and thus no stationary rainfall occurred near the mountain.

Two main conclusions can be drawn from these simulations. First, our BIGT experiments with constant environmental wind seem to fit pretty well with the theory developed in MR09 and MR10 (see Table 1). In fact, experiments BIGT3, BIGT4, BIGT5, and BIGT10 show stationary rainfall with moderate rainfall rates and slightly upstream rainfall peaks (cf. the right side in MR09's Figs. 15b and 16b); experiments BIGT6, BIGT7, and BIGT11 belong to a region of the parameter space characterized by moderate/large (BIGT6 and BIGT7) or moderate/small (BIGT11) downstream rainfall peaks (cf. MR10, their Fig. 3); and BIGT9 corresponds correctly to a region of nonstationary rainfall (MR09, their Fig. 15c). The solution response corresponding to the first two groups of experiments is represented in Fig. 1c, while the last case is illustrated in Fig. 1b. However, the estimated rainfall rates for the BIGT case are small compared with observed values.[2]

It appears that the inclusion of a low-level flow with no flow aloft produces deeper convective cells and a larger rainfall rate, and it puts the precipitation maximum on the upstream side of the mountain in this case. However, experiment BIGT9 and BIGT12 show that the low-level flow should be a proper combination of depth and intensity in order to produce an increase in the precipitation rate; too weak a wind speed or too shallow a layer of low-level flow does not stop the cold pool from propagating away from the mountain. When the cold

[2] However, here the maximum amount represents the longitudinal average across the channel and not the rainfall associated with a single system as in Caracena et al. (1979).

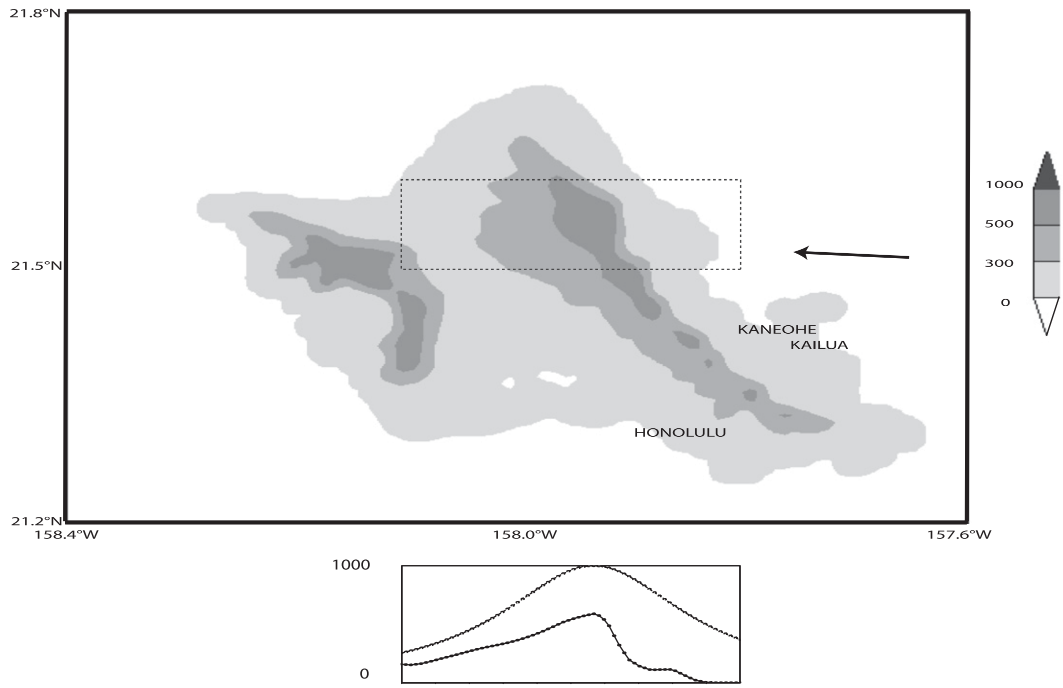

FIG. 5. As in Fig. 2 (with a different horizontal scale), but for the Oahu flood. The average mountain profile in the area of maximum rainfall, between 21.5° and 21.6°N and from 158.1° to 157.8°W, is shown for sake of comparison with the idealized profile.

pool is approximately balanced by the low-level flow, the induced upwind lifting combined with the absence of upper-level advection favors the generation of deep convective cells and gives a dramatic increase in the rainfall rate.

b. Oahu case

In this section we describe our simulations of the Oahu (Hawaii) flood of 1974 (Schroeder 1977). This case was chosen in order to explore rather different environmental conditions in an area vulnerable to heavy-rain events (Kodama and Barnes 1997; Lyman et al. 2005; among others); the topography, characterized by very steep slopes (Fig. 5), has different characteristic lengths from that of the Rockies in the area of the Big Thompson flood, and in contrast to the BIGT case, while the thunderstorms initiated at the ridge, the flooding occurred downwind of the ridge crest.

The flash floods caused by heavy thunderstorms on the morning of 19 April 1974 resulted in five deaths and \$3.9 million property damage in the Hawaiian islands. A peak rain rate of 114 mm in 1 h and a rainfall amount of 267 mm in 4 h was recorded on the northern side of the island (Schroeder 1977).

As in the BIGT case, the OAHU case is characterized by persistent, moderate easterly low-level flow toward the orography; however, we initially considered a sounding with a constant-wind $U = 10$ m s^{-1}. This value is comparable to the mean across-mountain wind component, calculated from the vertical profile below 500 hPa at 0200 local time (=UTC − 10 h), 19 April 1974, in Schroeder (1977), his Fig. 5, and shown in Fig. 6.

We started our analysis by initializing the model with the sounding from Lihue (21.98°N, 159.35°W; on the eastern side of Kauai island, west-northwest of Oahu) at 1200 UTC 19 April 1974, downloaded from the University of Wyoming website (http://weather.uwyo.edu/upperair/sounding.html). The sounding appeared to be absolutely unstable; consequently, our numerical simulation exhibited a large amount of convection everywhere in the domain. T. Schroeder (2010, personal communication) was of the opinion that the original sounding was not accurate.[3] Thus, we decided to initialize our model with the sounding in Schroeder (1977), his Fig. 6, modified by a slight smoothing (temperature and dewpoint temperature represented by the dashed lines in Fig. 6). A bell-shaped mountain with $h_m = 1000$ m and $a = 10$ km was used. Our numerical simulations indicated weak

[3] "This is pure speculation but it may be possible that the soundings were later adjusted . . . I recall there was some 'flap' about humidity sensors on NWS sondes back in the 70's. . ." (see also Wade 1994).

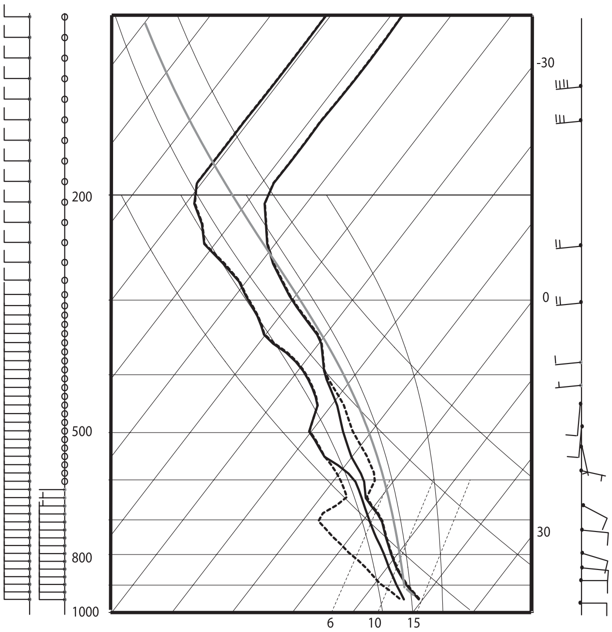

FIG. 6. The idealized profiles of temperature and dewpoint used in our experiments OAHU4, OAHU5 (solid, thick black lines), and OAHU1 (dashed, thick black lines) (the profiles for experiments OAHU2 and OAHU3 are a mixture of the two soundings; see text). The bold gray line represents the pseudoadiabatic curve of a parcel lifted from the surface in all experiments. The wind profiles used to initialize the atmosphere in experiments OAHU4 and OAHU5 are also shown on the left side of the figure together with the observed sounding from Schroeder (1977), their Fig. 5 (on the right).

precipitation compared to the observations (cf. experiment OAHU1 in Table 2 with the observed peak of approximately 50–100 mm h^{-1} during the period of the most intense rainfall, as shown in Schroeder 1977, his Fig. 8), while the maximum occurred slightly upstream of the mountain crest instead of the observed downstream location. To see if small changes in the sounding would produce larger rainfall rates, we removed the thermal inversion from 600 to 450 hPa (solid-line temperature profile with dashed-line dewpoint temperature profile in Fig. 6), which also had the effect of slightly increasing the value of CAPE (experiment OAHU2 in Table 2); again, the simulated convection was weak and the results from experiment OAHU1 were only marginally changed.

Taking into consideration the uncertainties in the humidity sounding, in the next experiment the dewpoint was increased with respect to experiment OAHU1 in the layer from 950 to 600 hPa (experiment OAHU3 in Table 2; dashed-line temperature profile with solid-line dewpoint profile in Fig. 6). As a result, a much larger rainfall rate (15 mm h^{-1}) was generated in the simulation, while the maximum remained confined upstream of the crest. Finally, when the modifications to both dewpoint and temperature were included in the sounding (solid lines in Fig. 6; experiment OAHU4 in Table 2), the precipitation rate did not change with respect to experiment OAHU3, while the rainfall maximum moved above the mountain crest.

To compare the model results with the theoretical results in MR09 and MR10, we note that the present simulations show a rainfall peak located mainly at the ridge crest or slightly upstream, as in Fig. 1c, consistent with MR10, their Fig. 2b (h_m/a = 0.10, h_m/LFC = 1.0–1.25). Concerning the rainfall rate, the comparison is more complex; however, the progressive increase of the nondimensional rainfall in experiments OAHU1–4 with increasing τ_a/τ_c is consistent with the rightward shift of the maximum nondimensional rainfall in going from MR10, their Fig. 2a (τ_a/τ_c = 3.3), to MR10, their Fig. 3a (τ_a/τ_c = 6.6).

As with the BIGT simulations, we have found that a key factor in the OAHU case is the presence of low-level flow toward the orography and relatively light cross-barrier flow in the middle troposphere. Again, when we considered a simulation with low-level flow and no flow aloft, the precipitation rate was much larger (experiment OAHU5 in Table 2). The setup of experiment OAHU5 differs from experiment OAHU4 only in terms of the wind profile: the wind speed is the same below 2900 m (U = 10 m s^{-1}), while above 4200 m it is equal to 0 (the profile was derived from the observations of the upstream across-mountain wind component); between 2900 and 4200 m, $U(z)$ is determined by a linear interpolation. As in the BIGT case the simulation with the above-described wind profile $U(z)$ increases the precipitation peak by

TABLE 2. As in Table 1, but for the OAHU case.

Expt	U m s^{-1}	h_m m	a km	CAPE J kg^{-1}	DCAPE J kg^{-1}	LFC m	N s^{-1}	τ_a/τ_c	h_m/a	h_m/LFC	(DCAPE)$^{1/2}/U$	NLFC/U	R_m mm h^{-1}	X_m km	10^2 $R_m/\rho U$	X_m/a
OAHU1	10	1000	10	650	650	1000	0.008	2.5	0.10	1.00	2.5	0.8	5	−1	1.0	−0.1
OAHU2	10	1000	10	850	650	1000	0.008	2.9	0.10	1.00	2.5	0.8	4	−3	0.8	−0.3
OAHU3	10	1000	10	950	560	800	0.008	3.1	0.10	1.25	2.4	0.6	15	−3	3.0	−0.3
OAHU4	10	1000	10	1150	605	800	0.008	3.4	0.10	1.25	2.5	0.6	16	0	3.2	0.0
OAHU5		1000	10	1150	605	800	0.008		0.10	1.25			34	8		0.8

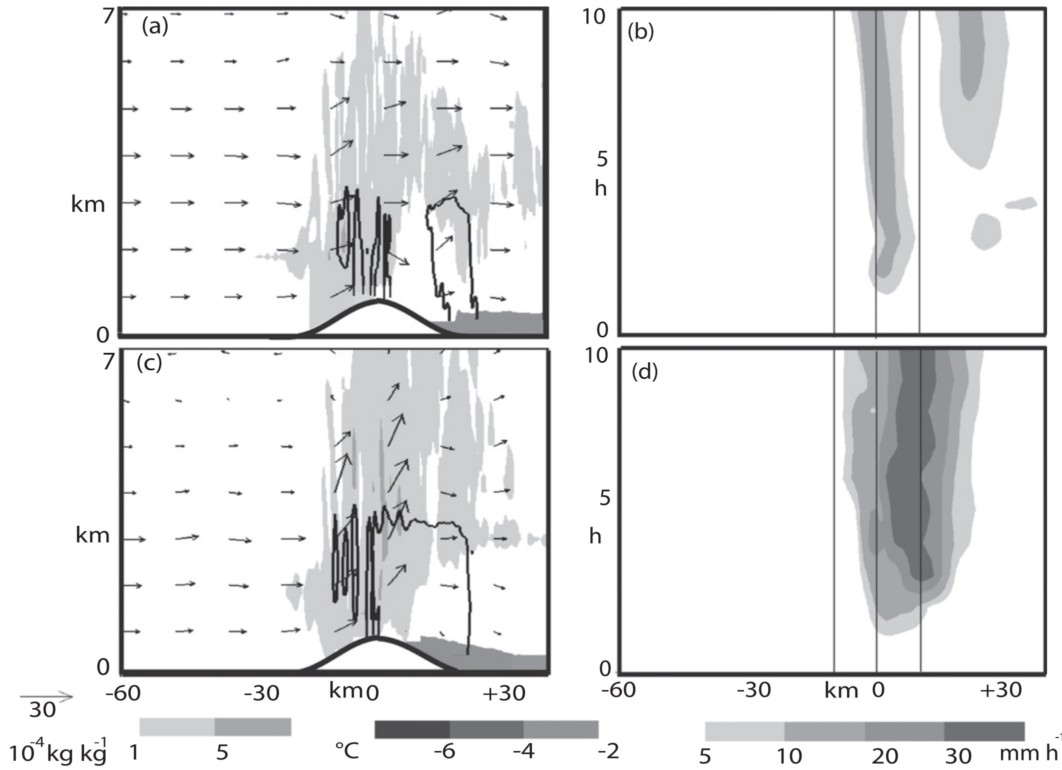

FIG. 7. As in Fig. 4, but for experiments (top) OAHU4 and (bottom) OAHU5. Rainwater content contour line is for 0.5×10^{-3} kg kg^{-1}.

a factor of more than 2 and it also shifts the simulated peak to the downwind side of the ridge crest, which is in better agreement with the observations.

Comparing simulations with U = const and with $U = U(z)$ in Fig. 7, one sees that the latter favors the vertical development of convective cells (Figs. 7c,d), while in the constant-wind case, Figs. 7a,b show that their vertical extent is more confined. Compared to the BIGT case, the cold pool in the $U = U(z)$ case is weaker (limited evaporative cooling was also noted in Schroeder 1977) and confined downstream of the ridge. Also, the leeside downward motion associated with the presence of a mountain wave in the OAHU4 case (Figs. 7a,b) suppresses the rainfall there (cf. Smith et al. 2009) and thus shifts the precipitation pattern upstream. As a consequence, in experiment OAHU5 the rainfall occurs downwind of the ridge crest, while in experiment OAHU4 the main maximum is confined to a very limited area at the ridge crest (and to a secondary maximum farther downstream associated with the "hydraulic jump" feature; see MR09, p. 1874). Finally, in experiment OAHU5 the simulated precipitation is more uniformly distributed along the mountain with some weak bands upstream of the mountain peak, while in experiment OAHU4 the rainfall is concentrated in banded features (Fig. 8), similar to those studied in Kirshbaum et al. (2007a,b).

c. Gard

This case has been studied in several papers (Delrieu et al. 2005; Davolio et al. 2006; Nuissier et al. 2008; Ducrocq et al. 2008; Bresson et al. 2009; Davolio et al. 2009; among others). The area affected by the flood was

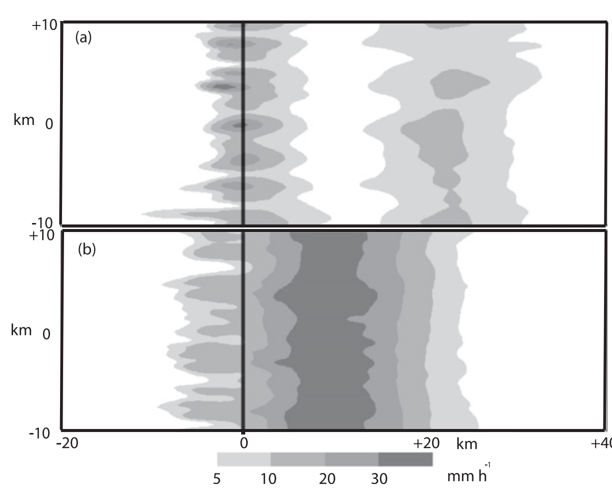

FIG. 8. Rainfall rates simulated near the mountain in experiments (a) OAHU4 and (b) OAHU5. The rainfall is calculated as the hourly average from $t = 5$ to $t = 10$ h. The vertical line represents the location of the ridge top.

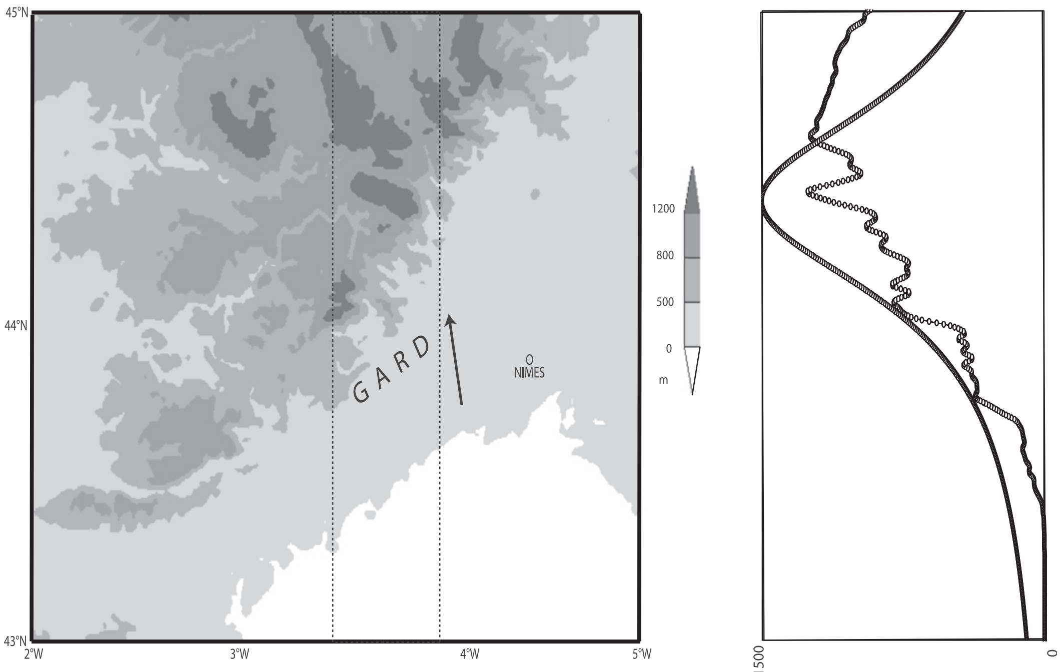

FIG. 9. As in Fig. 2 (with a different horizontal scale), but for the Gard flash flood. The average mountain profile in the area of maximum rainfall, between 3.4° and 3.9°E and from 43° to 45°N, is shown for sake of comparison with the idealized profile.

Gard, France, in the Cévennes–Vivarais region. The latter is characterized by a complex orography, the Cévennes mountains, elongated for about 60 km from southwest to northeast, with a maximum peak of about 1700 m (Fig. 9).

The 8–9 September 2002 flash flood resulted in 24 casualties and economic damage of about €1.2 billion. The event was particularly remarkable for the spatial extent of the rainfall, which was greater than 200 mm in 24 h over 5500 km^2, and its maximum daily values of 600–700 mm, with a peak of 140 mm h^{-1} (Delrieu et al. 2005). Most of the intense rainfall amount occurred slightly upstream in connection with a quasi-stationary mesoscale convective system.

The region was affected by a persistent moist and warm low-level flow. However, the meteorological features characterizing the event are significantly three dimensional, as the southerly flow from the Mediterranean Sea, which affects the southern part of the region, interacts with an easterly flow affecting its northern part (Nuissier et al. 2008) in proximity of highly complicated three-dimensional mountain barriers. Also, the situation is nonstationary, as the episode underwent three distinct phases, during which the large-scale circulation changed significantly (among the other factors, a cold front crossed the area from the west).

Thus, the limitations discussed in section 3 were particularly severe for this case study. Nonetheless it is desirable to know if some simplified set of physical factors could contain the essence of the Gard event. Davolio et al. (2009) conducted numerical experiments with the following simplification for the Gard case: an idealized 3D orography with the horizontally homogeneous upstream profiles computed by averaging the atmospheric variables of the ECMWF analyses over a domain of $2° \times 2°$ upstream of the mountains at the ''best initialization time'' of 0600 UTC 8 September 2002. Bresson et al. (2009) considered simplified longitudinally and vertically varying wind and moisture soundings but used the actual topography of the region in their numerical experiments. In our simplified framework, we initialized the model with the sounding from Nimes (43.86°N, 4.40°E) at 1200 UTC 8 September 2002 (the same as that chosen in Bresson et al. 2009), with a constant-wind speed $U = 10$ m s^{-1} (Fig. 10) and we used a bell-shaped mountain with $h_m =$ 1500 m and $a = 30$ km (experiment GARD1 in Table 3).

The result was a very small rainfall rate on the upstream side of the obstacle. To compare the simulation with the results shown in Bresson et al. (2009) (their simulation with a uniform moisture distribution), we increased the wind speed to $U = 15$ m s^{-1} (experiment GARD2 in Table 3). Rainfall rate increases and the model results (upstream quasi-stationary cells in Fig. 11a) qualitatively resemble those shown in Bresson et al. (2009), their Figs. 3 and 6. Moreover, both experiment GARD1 and

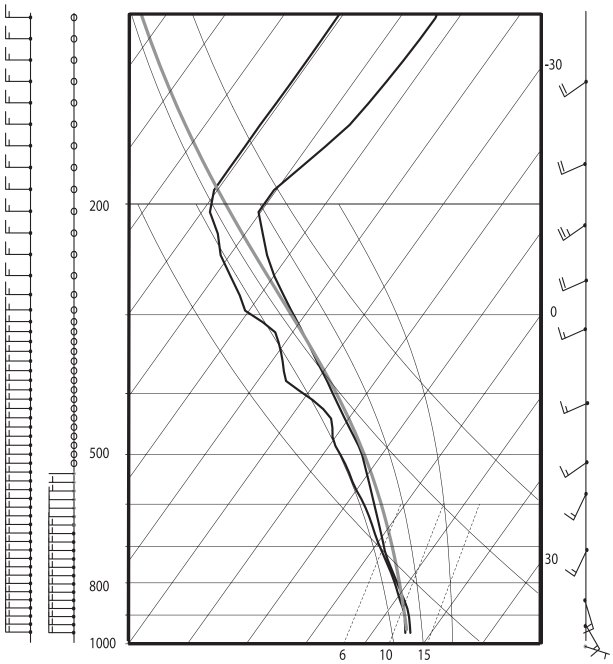

FIG. 10. The idealized profiles of temperature and dewpoint used in our experiments GARD1–5 (solid, thick black lines). The bold gray line represents the pseudoadiabatic curve of a parcel lifted from the surface. The wind profiles used to initialize the atmosphere in the experiments GARD2 and GARD3 are also shown on the left side together with the observed sounding from Delrieu et al. (2005), their Fig. 5 (on the right).

experiment GARD2 fit very well with MR10, their Fig. 2, as the corresponding points in the parameter space belong to a region of relatively small nondimensional rainfall ($\sim$1) and upstream location of the peak (Fig. 1c).

Motivated by the present experience with the BIGT and OAHU simulations, we tested the role of a wind profile $U(z)$ by setting $U = 15$ m s^{-1} below 3400 m and $U = 0$ above 5500 m, which reproduces the observed vertical profile of the across-mountain wind component (experiment GARD3 in Table 3). Figure 11 compares the constant-wind case experiment GARD2 (top) with low-level-flow-only case experiment GARD3 (bottom): stationary rainfall was simulated upstream of the mountain in both cases, and the rainfall rate was similar in the two experiments (Table 3). A notable difference with respect to the BIGT and OAHU simulations is that no cold pool is generated (this is a consequence of the small values of DCAPE) and relatively shallow convective cells. The main change due to the wind profile $U(z)$ is the removal of the gravity wave structure in the upper levels above the mountain (the wave structure is in evidence below $\sim$5 km; see Fig. 11c). In contrast with the OAHU case, along-flow rainbands are apparent in both experiment GARD2 and GARD3 (not shown); thus, we infer that the development of deep convection with a cold pool and the elimination of mountain waves are necessary in order to remove the bands and makes the precipitation more uniform in the along-mountain direction (consistent with Kirshbaum et al. 2007a,b).

To look for an optimal wind configuration that could significantly enhance the precipitation rate, additional experiments with different wind profiles were performed. For example, we set $U = 15$ m s^{-1} below 2700 m and $U = 0$ above 4700 m (experiment GARD4 in Table 3)—that is, slightly reducing the depth of the low-level jet with respect to experiment GARD3—while in experiment GARD5 (Table 3) we initialized the model with the same wind profile used in experiment OAHU5. However, none of these simulations showed any relevant change in the solution characteristics. Thus, our conclusion is that in this low-CAPE/DCAPE case the presence of the low-level flow with weak winds aloft does not significantly affect the precipitation in our simplified numerical experiments.

Davolio et al. (2009) found a response in the form of an upwind propagating cold pool with convection triggered at the leading edge. The sounding used by Davolio et al. (the relative humidity is shown in their Fig. 1, before an increase of about 13% in specific humidity is applied to the boundary layer; the wind profile is shown in their Fig. 2) appears rather different from the observed profile we used, as the low-level-flow is much weaker (about 5 m s^{-1} of across-mountain component) and is directed toward the mountain only in a shallow layer (2000 m deep above the ground), while CAPE is larger (1100 J kg^{-1}). A weaker U and larger CAPE corresponds to a value of $\tau_a/\tau_c \gg 1$, which favors the generation of an

TABLE 3. As in Table 1, but for the GARD case.

Expt	U m s^{-1}	h_m m	a km	CAPE J kg^{-1}	DCAPE J kg^{-1}	LFC m	N s^{-1}	τ_a/τ_c	h_m/a	h_m/LFC	(DCAPE)$^{1/2}/U$	NLFC$/U$	R_m mm h^{-1}	X_m km	10^2 $R_m/\rho U$	X_m/a
GARD1	10	1500	30	180	200	1500	0.01	4.0	0.05	1.00	1.4	1.8	5	−19	1.0	−0.6
GARD2	15	1500	30	180	200	1500	0.01	2.7	0.05	1.00	0.9	1.2	8	−10	1.1	−0.3
GARD3		1500	30	180	200	1500	0.01		0.05	1.00			11	−9		−0.3
GARD4		1500	30	180	200	1500	0.01		0.05	1.00			11	−16		−0.5
GARD5		1500	30	180	200	1500	0.01		0.05	1.00			8	−15		−0.5

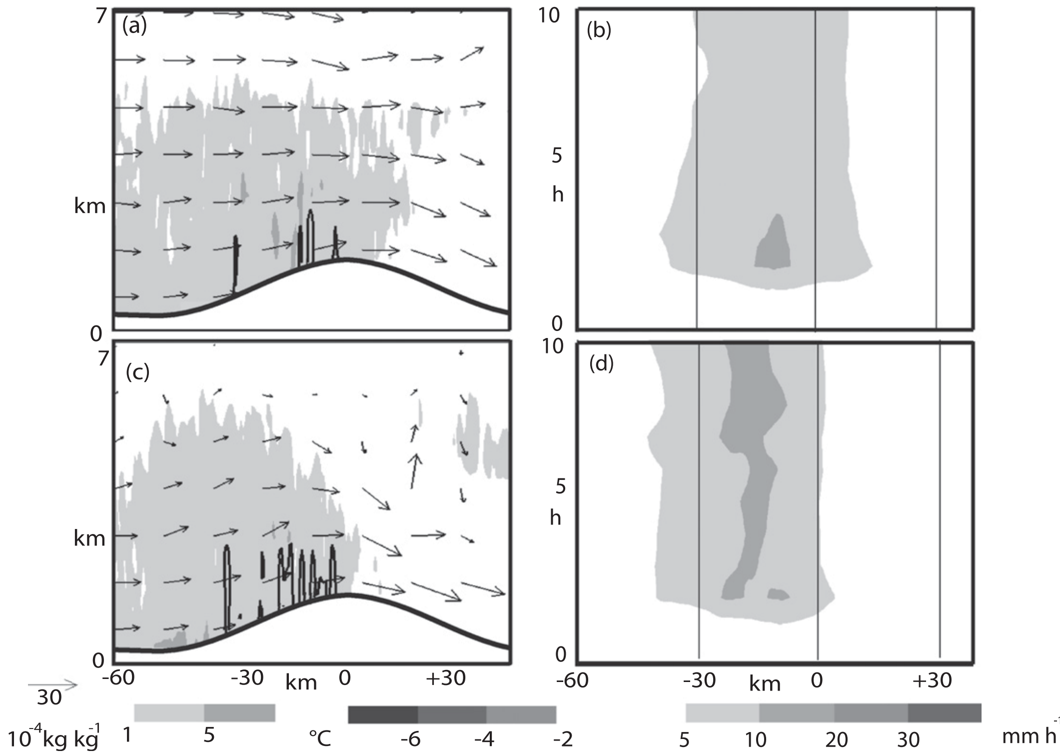

FIG. 11. As in Fig. 7, but for experiments (top) GARD2 and (bottom) GARD3.

upstream propagating cold pool (Fig. 1b). The discussion following the BIGT case suggests that for an optimal combination of depth and intensity of the low-level flow, the cold pool can be approximately balanced and an increase in the precipitation rate is produced. The sounding proposed in Davolio et al. (2009) seems to satisfy such conditions approximately, although with a slightly larger cold pool propagation speed with respect to the environmental wind speed. Finally, we used their thermodynamic sounding within our simplified setup and we found (not shown) effectively an upstream propagating cold pool both for a constant-wind profile ($U = 5$ m s^{-1}) and in presence of a low-level jet with calm aloft (in the latter case a larger rainfall was produced). Also, we noted a strong sensitivity to the environmental wind speed (an approximate balance between the cold pool and the environmental wind was simulated for a uniform wind profile with $U = 7$ m s^{-1}).

4. Conclusions

In the present paper we examined several idealized simulations relative to case studies of orographic convective heavy rainfall, which were performed using a setup basically as that described in MR09. Here we used a constant-wind profile and profiles of temperature and humidity representative of the observed upstream environmental conditions, somehow different from the Weisman–Klemp sounding used in our previous idealized studies.

We obtained results in line with the dimensional analysis discussed in MR09 and MR10. However, with respect to the observations, much smaller rainfall rates were simulated and we found that the uniform wind profiles used to initialize the model had to be modified in order to obtain larger rainfall rates. Specifically we found that low-level flow toward the mountain with weak wind aloft can double simulated rain rates.

Our basic point of reference is the case of Big Thompson flood. In this case, we considered a constant-wind profile, and found that the simulated precipitation characteristics agree fairly well with the theory developed in MR09–MR10, but did not fit well with the observations. We tried to modify different parameters in the thermodynamic sounding by removing inversion layers or dry midlevels, or making changes in low-level moisture within observational uncertainty, but we could not obtain anything significantly different. A major difference came when we considered a sounding with a low-level flow toward the mountain and decreasing to zero aloft. With the latter wind profile, the simulated precipitation is in the correct location, upstream of the mountain ridge, and intense (although much smaller than the observations). When we considered the same wind profile but with a weaker low-level flow, the simulation produced a cold pool propagating away from the mountain and, in that case, no steady-state solution was obtained.

Other cases were then analyzed. The Oahu case showed results basically consistent with the Big Thompson case. On the other hand, for the Gard case, the wind variation with height was not able to significantly intensify the rainfall. We believe that this lack of influence of wind shear is due to the very small CAPE, thus the convection is shallow and the cell development cannot benefit for the weaker wind aloft; also DCAPE is small, thus the cold pool simulated in this simplified context, which in the other two cases with wind shear was generally deep and remained confined close to the mountain, was very weak. Other studies of the Gard case (Davolio et al. 2009) using a sounding with greater values of CAPE produced results more in line with the Big Thompson and Oahu cases.

Although not reported on here, in an attempt to explore more general situations we analyzed two other episodes of orographic convective rainfall. In one case, we considered a sounding representative of heavy-rain conditions over the south-facing (upstream) slopes of the island of Hawaii (sounding in Lihue of 0000 UTC 19 November 2000; see Kodama and Barnes 1997). In another case, we considered a sounding of 31 May 2008 from the Terrain-influenced Monsoon Rainfall Experiment (TiMREX), which is a field program conducted in the complex orography regions of southern Taiwan in 2008. In both cases, the low-level jet and calm aloft are effective in more than doubling precipitation.

The larger rainfall in the simulations with a wind profile $U(z)$ can be attributed to two different factors: 1) convective cells are deeper and stronger than those in the constant-wind case and 2) cells are not moving with respect to the mountain (this factor is usually mentioned in observational studies); as the cells go up into upper layers characterized by very weak wind, they are no longer advected with respect to the mountain and thus produce a more stationary rainfall pattern.

In conclusion, the results of the present study show that too few parameters were considered in our theory, as at least wind variation with height needs to be considered. The effect of the wind profile will be explored more deeply in a following article where we will report on experiments using the Weisman–Klemp sounding but with shear profiles consistent with the present case-study simulations.

REFERENCES

Bresson, R., D. Ricard, and V. Ducrocq, 2009: Idealized mesoscale numerical study of Mediterranean heavy precipitating convective systems. *Meteor. Atmos. Phys.,* **103,** 45–55.

Bryan, G. H., and J. M. Fritsch, 2002: A benchmark simulation for moist nonhydrostatic models. *Mon. Wea. Rev.,* **130,** 2917–2928.

Buzzi, A., and L. Foschini, 2000: Mesoscale meteorological features associated with heavy precipitation in the southern Alpine region. *Meteor. Atmos. Phys.,* **72,** 131–146.

Caracena, F. R., A. Maddox, L. R. Hoxit, and C. F. Chappell, 1979: Mesoanalysis of the Big Thompson storm. *Mon. Wea. Rev.,* **107,** 1–17.

Chappell, C. F., 1986: Quasi-stationary convective events. *Mesoscale Meteorology and Forecasting,* P. S. Ray, Ed., Amer. Meteor. Soc., 289–310.

Davis, R. S., 2001: Flash flood forecast and detection methods. *Severe Convective Storms, Meteor. Monogr.,* No. 50, Amer. Meteor. Soc., 481–525.

Davolio, S., A. Buzzi, and P. Malguzzi, 2006: Orographic influence on deep convection: Case study and sensitivity experiments. *Meteor. Z.,* **15,** 215–223.

——, ——, and ——, 2009: Orographic triggering of long-lived convection in three dimensions. *Meteor. Atmos. Phys.,* **103,** 35–44.

Delrieu, G., and Coauthors, 2005: The catastrophic flash-flood event of 8–9 September 2002 in the Gard region, France: A first case study for the Cévennes–Vivarais Mediterranean Hydrometeorological Observatory. *J. Hydrometeor.,* **6,** 34–52.

Ducrocq, V., O. Nuissier, D. Ricard, C. Lebeaupin, and T. Thouvenin, 2008: A numerical study of three catastrophic precipitating events over western Mediterranean region (southern France). Part II: Mesoscale triggering and stationarity factors. *Quart. J. Roy. Meteor. Soc.,* **134,** 131–145.

Gilmore, M., and L. J. Wicker, 1998: The influence of midtropospheric dryness on supercell morphology and evolution. *Mon. Wea. Rev.,* **126,** 943–958.

Grossman, R. L., and D. R. Durran, 1984: Interaction of low-level flow with the Western Ghat Mountains and offshore convection in the summer monsoon. *Mon. Wea. Rev.,* **112,** 652–672.

Kirshbaum, D. J., G. H. Bryan, R. Rotunno, and D. R. Durran, 2007a: The triggering of orographic rainbands by small-scale topography. *J. Atmos. Sci.,* **64,** 1530–1549.

——, R. Rotunno, and G. H. Bryan, 2007b: The spacing of orographic rainbands triggered by small-scale topography. *J. Atmos. Sci.,* **64,** 4222–4245.

Kodama, K., and G. M. Barnes, 1997: Heavy rain events over the south-facing slopes of Hawaii: Attendant conditions. *Wea. Forecasting,* **12,** 347–367.

Lyman, R. E., T. A. Schroeder, and G. M. Barnes, 2005: The heavy rain event of 29 October 2000 in Hana, Maui. *Wea. Forecasting,* **20,** 397–414.

Maddox, R. A., L. R. Hoxit, C. F. Chappell, and F. Caracena, 1978: Comparison of meteorological aspects of the Big Thompson and Rapid City flash floods. *Mon. Wea. Rev.,* **106,** 375–389.

Miglietta, M. M., and R. Rotunno, 2006: Further results on moist nearly neutral flow over a ridge. *J. Atmos. Sci.,* **63,** 2881–2897.

——, and ——, 2009: Numerical simulations of conditionally unstable flows over a ridge. *J. Atmos. Sci.,* **66,** 1865–1885.

——, and ——, 2010: Numerical simulations of low-CAPE flows over a mountain ridge. *J. Atmos. Sci.,* **67,** 2391–2401.

Neiman, P. J., F. M. Ralph, A. B. White, D. E. Kingsmill, and P. O. G. Persson, 2002: The statistical relationship between upslope flow and rainfall in California's coastal mountains: Observations during CALJET. *Mon. Wea. Rev.,* **130,** 1468–1492.

Nuissier, O., V. Ducrocq, D. Ricard, C. Lebeaupin, and S. Anquetin, 2008: A numerical study of three catastrophic precipitating events over Southern France. I: Numerical framework and synoptic ingredients. *Quart. J. Roy. Meteor. Soc.,* **134,** 111–130.

Pontrelli, M. D., G. H. Bryan, and J. M. Fritsch, 1999: The Madison County, Virginia, flash flood of 27 June 1995. *Wea. Forecasting,* **14,** 384–404.

Richard, E., A. Buzzi, and G. Zängl, 2007: Quantitative precipitation forecasting in the Alps: The advances achieved by the Mesoscale Alpine Programme. *Quart. J. Roy. Meteor. Soc.,* **133,** 831–846.

Romero, R., C. A. Doswell III, and C. Ramis, 2000: Mesoscale numerical study of two cases of long-lived quasi-stationary convective systems over eastern Spain. *Mon. Wea. Rev.,* **128,** 3731–3751.

Rotunno, R., and R. Ferretti, 2001: Mechanisms of intense Alpine rainfall. *J. Atmos. Sci.,* **58,** 1732–1749.

——, and R. A. Houze, 2007: Lessons on orographic precipitation from the Mesoscale Alpine Programme. *Quart. J. Roy. Meteor. Soc.,* **133,** 811–830.

Schroeder, T. A., 1977: Meteorological analysis of an Oahu flood. *Mon. Wea. Rev.,* **105,** 458–468.

Senesi, S., P. Bougeault, J.-L. Chèze, P. Cosentino, and R.-M. Thepenier, 1996: The Vaison-La-Romaine flash flood: Mesoscale analysis and predictability issues. *Wea. Forecasting,* **11,** 417–442.

Smith, R. B., P. Schafer, D. J. Kirshbaum, and E. Regina, 2009: Orographic precipitation in the tropics: Experiments in Dominica. *J. Atmos. Sci.,* **66,** 1698–1716.

Wade, C. G., 1994: An evaluation of problems affecting the measurements of low relative humidity on the United Stated radiosondes. *J. Atmos. Oceanic Technol.,* **11,** 687–700.

Wang, J.-J., R. M. Rauber, H. T. Ochs III, and R. E. Carbone, 2000: The effects of the island of Hawaii on offshore rainband evolution. *Mon. Wea. Rev.,* **128,** 1052–1069.

Weisman, M. L., and J. B. Klemp, 1982: The dependence of numerically simulated convective storms on vertical wind shear and buoyancy. *Mon. Wea. Rev.,* **110,** 504–520.

Yoshizaki, M., and Y. Ogura, 1988: Two- and three-dimensional modeling studies of the Big Thompson storm. *J. Atmos. Sci.,* **45,** 3700–3722.

Yu, C.-K., and Y.-H. Hsieh, 2009: Formation of the convective lines off the mountainous coast of southeastern Taiwan: A case study of 3 January 2004. *Mon. Wea. Rev.,* **137,** 3072–3091.

——, D. P. Jorgensen, and F. Roux, 2007: Multiple precipitation mechanisms over mountains observed by airborne Doppler radar during MAP IOP5. *Mon. Wea. Rev.,* **135,** 955–984.